

Viscoelastic Dissipation Stabilizes Cell Shape Changes during Tissue Morphogenesis

Highlights

- Myosin-driven and optical forces reveal the dissipative mechanics of cell contacts
- Deformations of cell contacts are stabilized by dissipation on the minute timescale
- Longer force application yields less reversible deformations
- Dissipation and thus reversibility of deformations rely partly on actin turnover

Authors

Raphaël Clément, Benoît Dehapiot,
Claudio Collinet, Thomas Lecuit,
Pierre-François Lenne

Correspondence

raphael.clement@univ-amu.fr (R.C.),
pierre-francois.lenne@univ-amu.fr
(P.-F.L.)

In Brief

Clément et al. investigate the mechanics underlying the irreversibility of morphogenetic deformations. They show that deformations caused by contractile pulses of myosin II or by optical tweezers are stabilized by dissipation on the minute timescale. Inhibiting actin turnover reduces dissipation and yields more reversible deformations.

Viscoelastic Dissipation Stabilizes Cell Shape Changes during Tissue Morphogenesis

Raphaël Clément,^{1,3,*} Benoît Dehapiot,¹ Claudio Collinet,¹ Thomas Lecuit,^{1,2} and Pierre-François Lenne^{1,*}

¹Aix-Marseille Univ., CNRS, IBDM, Marseille, France

²Collège de France, 11 place Marcelin Berthelot, Paris, France

³Lead Contact

*Correspondence: raphael.clement@univ-amu.fr (R.C.), pierre-francois.lenne@univ-amu.fr (P.-F.L.)

<http://dx.doi.org/10.1016/j.cub.2017.09.005>

SUMMARY

Tissue morphogenesis relies on the production of active cellular forces. Understanding how such forces are mechanically converted into cell shape changes is essential to our understanding of morphogenesis. Here, we use myosin II pulsatile activity during *Drosophila* embryogenesis to study how transient forces generate irreversible cell shape changes. Analyzing the dynamics of junction shortening and elongation resulting from myosin II pulses, we find that long pulses yield less reversible deformations, typically a signature of dissipative mechanics. This is consistent with a simple viscoelastic description, which we use to model individual shortening and elongation events. The model predicts that dissipation typically occurs on the minute timescale, a timescale commensurate with that of force generation by myosin II pulses. We test this estimate by applying time-controlled forces on junctions with optical tweezers. Finally, we show that actin turnover participates in dissipation, as reducing it pharmacologically increases the reversibility of contractile events. Our results argue that active junctional deformation is stabilized by actin-dependent dissipation. Hence, tissue morphogenesis requires coordination between force generation and dissipation.

INTRODUCTION

The course of animal development is a succession of morphogenetic movements, which require the activity of force-generating cortical components that exert mechanical forces at the cellular scale [1, 2]. Classic examples include cell intercalation, in which polarized activity of myosin II (MyoII) motors drives tissue elongation [3, 4], or apical constriction, in which MyoII drives tissue folding and invagination [5]. At the cell level, deformations rely on transient forces resulting from the pulsatile activity of MyoII [5–8]. A key question is thus how these transient forces can result in persistent deformations. This requires a mechanical understanding of how cells and tissues dissipate energy and thereby escape elastic recoil once contractile stresses (e.g., forces) are no longer applied. Indeed, cells and tissues are neither purely

elastic nor viscous but viscoelastic. Whereas elasticity provides robustness to short-lived stresses, dissipation allows the system to change shape without dramatic stress accumulation, which can threaten cellular integrity [9]. Thus, a likely mechanism to stabilize deformation is the gradual dissipation of elastic energy during the morphogenetic process [9]. Dissipation should therefore occur on timescales typically shorter, or commensurate with, but definitely not much longer than the timescale of force generation. Hence, it is often assumed that tissues behave as fluids on developmental timescales [10, 11]. Experimentally, the viscoelastic nature of single cells or cell assemblies have been assessed with a variety of techniques [12–15], and recent works using suspended epithelial monolayers [16] confirm that dissipation occurs upon application of a constant deformation, typically on the minute timescale [17]. Yet very few studies involve direct mechanical measurements *in vivo* in the context of morphogenesis. In a previous study using the *Drosophila* embryonic epithelium as a model system, we delineated the mechanics of cell contacts at short timescales, typically below a few seconds, showing that the response was mainly elastic and damped by fluid friction in the cytosol [18]. However, longer timescales remain largely unexplored, due to the technical challenge of actively probing cell mechanics in live embryos over long periods of time. Thus, a mechanical analysis at morphogenetic timescales and an estimate of the relevant dissipation timescales in a morphogenetically active tissue are still lacking.

Here, we take advantage of the irreversible shortening and elongation of cell junctions of the *Drosophila* germband in response to pulsatile myosin II activity to estimate the typical timescale of dissipation at cell contacts. Thereby, we sought to understand how transient forces generate irreversible deformation during this morphogenetic process.

Planar-polarized MyoII activity was shown to drive cell intercalation and participate in tissue extension in the germband [3, 4]. Oscillations, or pulses, of MyoII activity along junctions aligned with the dorso-ventral axis (Figure 1A) were shown to gradually shorten junctions, acting as a “mechanical ratchet” [8], and eventually resulting in the disappearance of vertical cell contacts (Figures 1B, 1D, and 1F). Similar MyoII pulsations, located in adjacent anterior and posterior cells in the vicinity of a junction’s vertices, were later shown to favor the formation and gradual elongation of new junctions along the antero-posterior axis (Figures 1C, 1E, and 1G) [19]. Previous studies have shown that efficient remodeling requires robust activation of MyoII in junctions [8, 20, 21], and whereas it is clear that MyoII is required to generate the force driving deformation, the mechanism by which

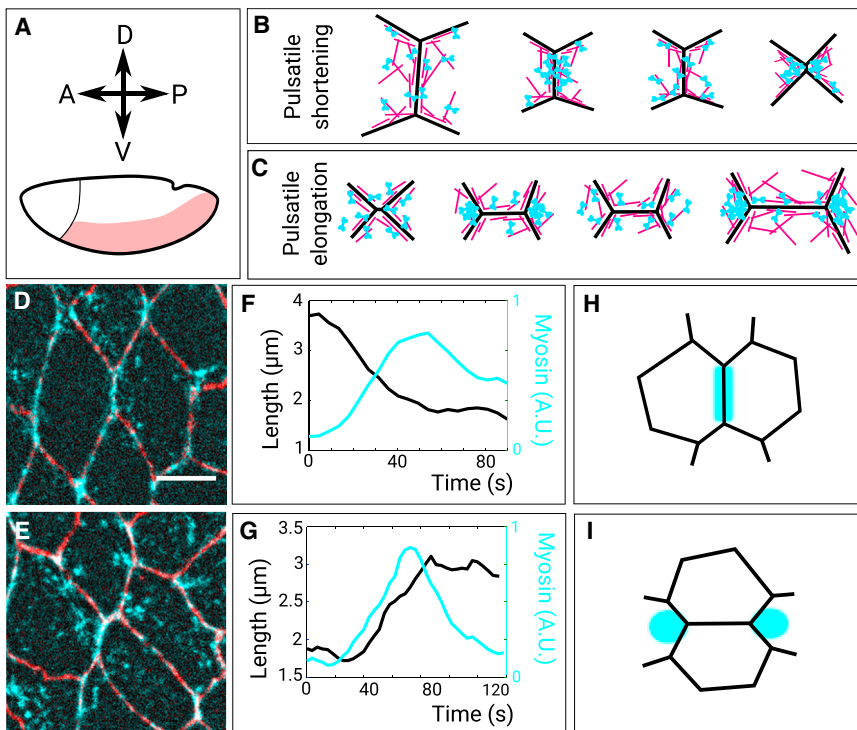


Figure 1. Junction Shortening and Elongation by MyoII Polarized Activity

(A) Schematics of the germband of the *Drosophila* embryo. A, P, D, and V symbolize the anterior, posterior, dorsal, and ventral directions.

(B) Cartoon of junction shortening driven by MyoII pulsatile activity. Actin is in magenta and MyoII in cyan.

(C) Cartoon of junction elongation driven by MyoII pulsatile activity. Actin is in magenta and MyoII in cyan.

(D) Junction undergoing shortening in the germband (E-cadherin, red; MyoII, cyan). MyoII is recruited at the junction. The scale bar represents 5 μm .

(E) Junction undergoing elongation in the germband. MyoII is recruited in the anterior and posterior cells, in the vicinity of vertices of newly forming junctions.

(F) Shortening dynamics during a pulse of junctional MyoII.

(G) Elongation dynamics during a pulse of MyoII located in the vicinity of vertices.

(H) Region analyzed to measure MyoII activity during shortening.

(I) Region analyzed to measure MyoII activity during elongation.

the resulting deformations are stabilized remains elusive. In the following, we introduce a minimal viscoelastic model of the so-called mechanical ratchet, which shows that active MyoII-driven deformations can be stabilized by dissipation. Analyzing junctional shortening and elongation in response to pulsatile forces generated by MyoII, we estimate the typical timescale of dissipation, which separates the elastic, reversible regime from the viscous, irreversible regime. We find that it is typically one minute and confirm this estimate with optical tweezers experiments in which a controlled external force is applied to junctions. Finally, we show that pharmacological reduction of actin turnover limits dissipation, so that contractile events in perturbed embryos are overall more reversible.

RESULTS

Our working hypothesis is that cell junctions are viscoelastic with a short-term elastic response and a long-term viscous response due to dissipation, allowing deformations generated by transient MyoII activity to be stabilized. Note that cell junctions, whose cortex consists of a complex and dynamic network of actin filaments that turn over and are crosslinked by a number of linkers [22], are likely to undergo dissipation on a distribution of timescales. For the sake of simplicity, we assume in the following that dissipation occurs on a single typical timescale τ .

Junction length dynamics during contractile pulses is correlated with the fluctuation of MyoII intensity [5, 8], which is known to generate forces at junctions [23]. Therefore, we ultimately want the model to predict the associated dynamics of MyoII intensity $M(t)$ and junction length $l(t)$. Because a mechanical model relates force to deformation, we first need to relate MyoII intensity to force $f(t)$. MyoII recruitment at the cortex requires

activation and is used as a proxy for motor activity. Whereas it is largely assumed that force increases with MyoII activity, the precise scaling between MyoII and force production is unknown. For the sake of simplicity, we assume in the following that force is proportional to the excess of MyoII (with respect to MyoII base level M_0 observed in absence of pulses), so that $f = \pm \alpha(M - M_0)$. The \pm sign stands for shortening ($-$) or elongation ($+$). M_0 represents the amount of MyoII required to maintain constant junction length so that the junction is at rest when $M = M_0$. In practice, we assume that M_0 is the minimum of $M(t)$, which is consistent with junctions being at rest in the absence of pulses. Finally, α is an unknown scaling factor. From there, the dynamics of a viscoelastic junction submitted to MyoII-driven shortening or elongation is given by the following reformulation of the Maxwell model of viscoelasticity (see STAR Methods for details):

$$\pm \kappa_\alpha \dot{l} = \dot{m} + \frac{m}{\tau}. \quad (\text{Equation 1})$$

In Equation 1, κ_α is the ratio between the elastic modulus κ and the constant α , and $m = M - M_0$. Dots denote time derivatives, so that \dot{l} is the rate of elongation and \dot{m} the rate of MyoII recruitment. Note that, here, we neglect variations of tension in adjacent junctions as well as the contribution of viscous drag in the cytosol, which occurs on timescales much shorter than MyoII fluctuations [18]. The model has two free parameters: κ_α , which controls how much MyoII can elastically deform a junction, and τ , the typical dissipation timescale. In the case of shortening, M is MyoII fluorescent intensity measured in the vicinity of the junction (Figure 1H), where it is geometrically the most effective to exert a shortening force. This view is supported by apical cell constriction events occurring prior to mesoderm

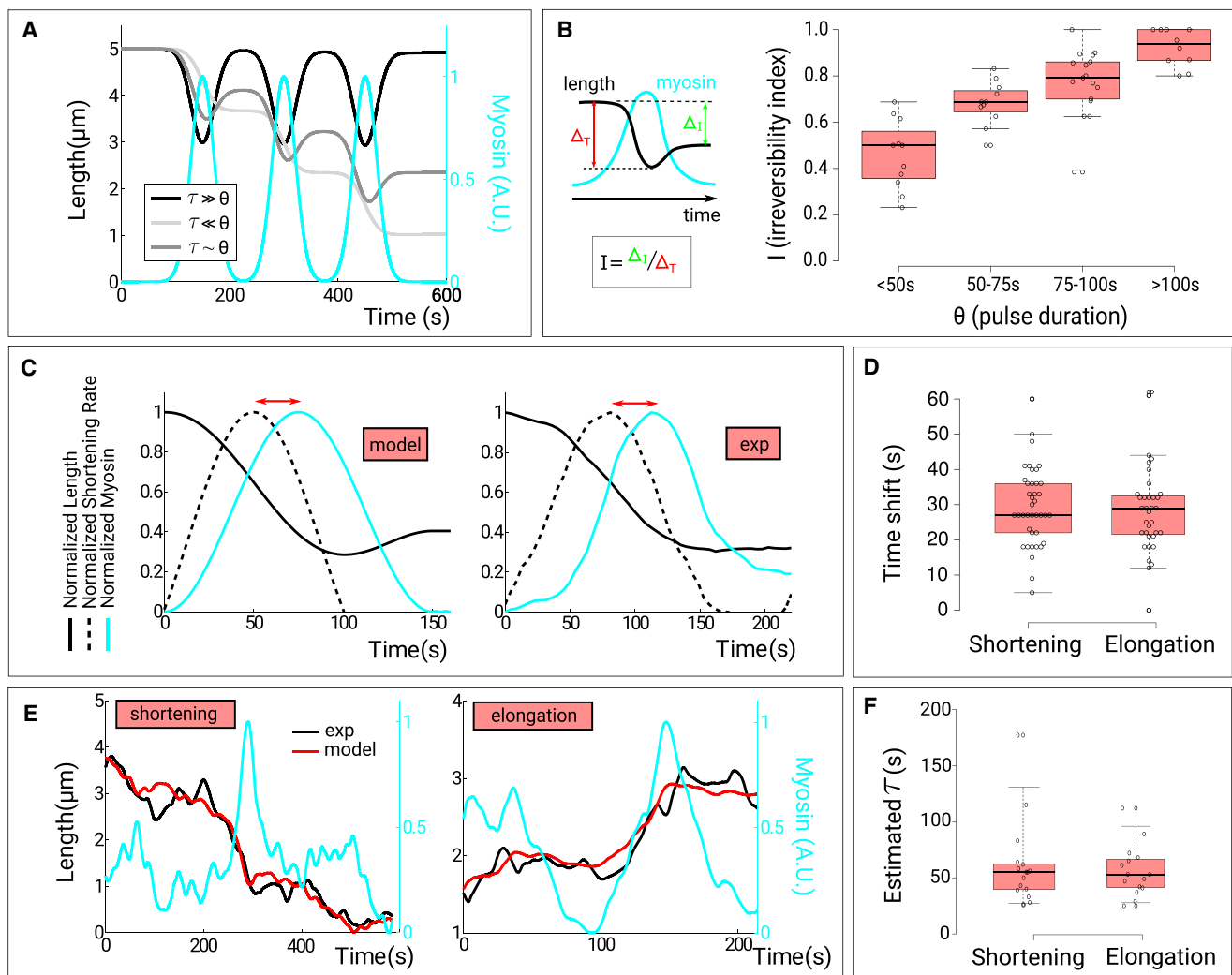


Figure 2. Viscoelastic Analysis of Contractile Pulses

(A) Shortening dynamics of a model viscoelastic junction in response to artificial Gaussian pulses. Black, $\tau = 1\text{h} \gg \theta$ (elastic regime); light gray, $\tau = 1\text{s} \ll \theta$ (viscous regime); dark gray, $\tau = 1\text{min} \sim \theta$ (intermediate regime).

(B) Left: Cartoon of the irreversibility index I , defined as the ratio between the irreversible deformation and the maximal deformation. Right: Irreversibility index I/θ increases with pulse duration θ ($n = 49$ from 5 embryos). Center lines of boxes show the medians; boxes limits indicate the 25th and 75th percentiles; and whiskers extend 1.5 times the interquartile range from the 25th and 75th percentiles.

(C) Time shift between the peak of deformation rate (here, shortening rate, dotted line) and the peak of MyoII activity (cyan). The former is ahead of the latter, both in a model pulse (left panel) and in experiments (right panel).

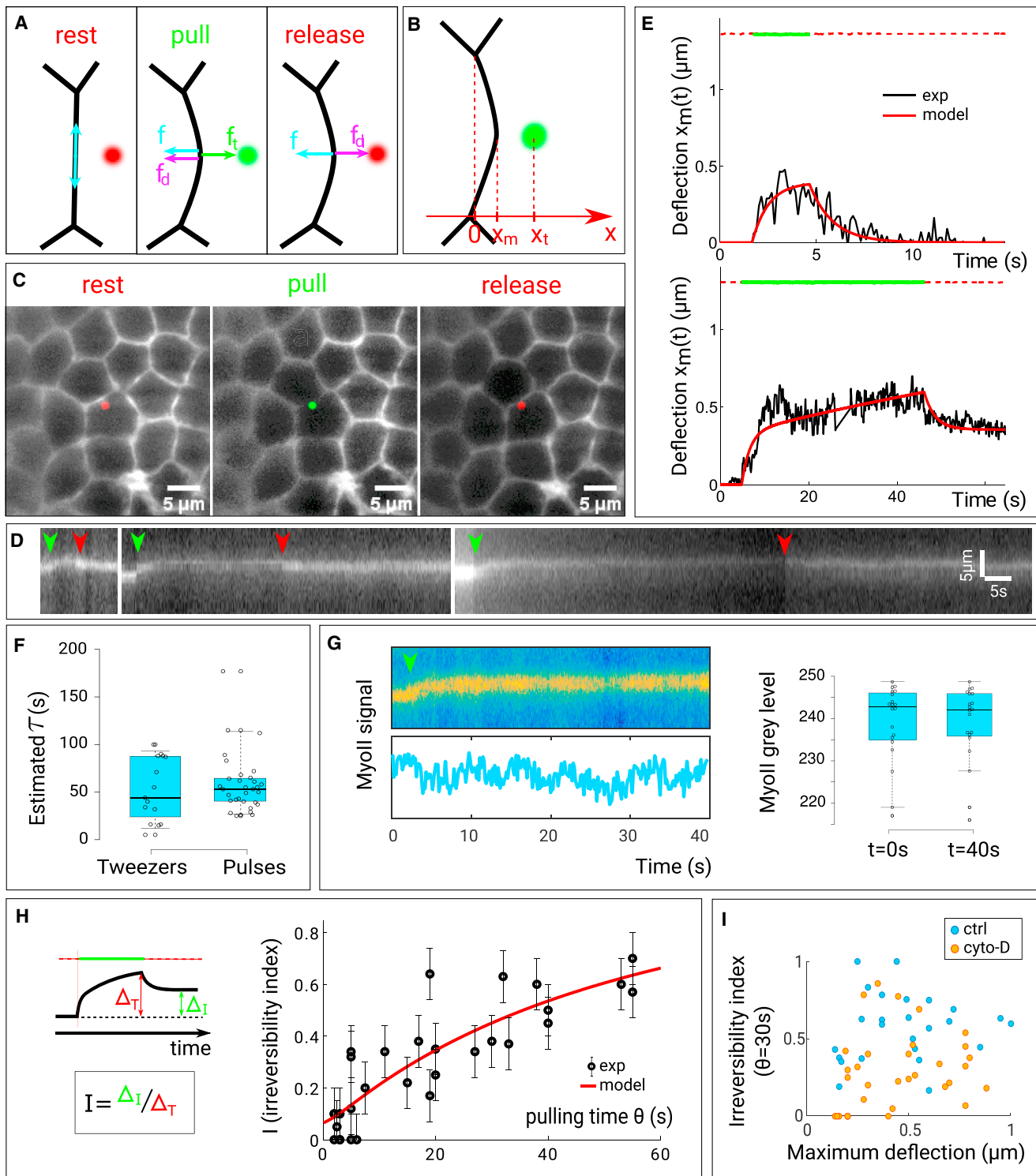
(D) Boxplot of the time shift between the peak of deformation rate and the peak of MyoII activity, measured for shortening events ($n = 40$ from 4 embryos) and elongation events ($n = 35$ from 3 embryos).

(E) Fit of junction shortening (left panel) and junction elongation (right panel) using the experimental MyoII signals depicted in Figures 1H and 1I as input for the model.

(F) Estimates of τ extracted from multiple fits of experiments, both for shortening ($n = 16$ from 3 embryos) and elongation ($n = 15$ from 3 embryos).

invagination, where MyoII accumulation in the medial part of the cell essentially shrinks cell area, with a mild effect on junction length. Importantly, this does not imply that MyoII from the medial region plays no role in junction shortening, as MyoII is known to flow toward junctions from the medial region [8]. In the case of elongation, junctions have very low MyoII levels, and we measure MyoII intensity M in adjacent anterior and posterior cells in the vicinity of vertices (Figure 1I), where it was shown to drive the growth of the new junction [19, 24].

The model is, in essence, timescale dependent. It is expected that the longer a force is applied, the less reversible the resulting deformation should be. Conversely, the shorter the dissipation timescale is, the faster one will observe irreversible deformations. This is illustrated in Figure 2A, where we show the predicted response of a junction to artificial MyoII pulses in three extreme scenarios. As expected, when the timescale of dissipation τ is much longer than the pulse duration θ (that is, when $\tau \gg \theta$), the response is mainly elastic and deformations are

**Figure 3. Viscoelastic Analysis of Optical Tweezers Experiments**

(A) Cartoon of the pull-release sequence and of the subsequent forces in the optical tweezers experiments. The trap is initially off (red), then switched on (green), and switched off again (red). Forces displayed are the restoring force f , the drag force f_d , and the trap force f_t .

(B) Cartoon of deflection quantification. We monitor deflections along the x axis, perpendicular to the junction. x_m is the junction position and x_t the optical trap position.

(C) Time-lapse sequence of a pull-release experiment, in which the junction is held for approximately 50 s.

(legend continued on next page)

essentially reversible, with complete recovery between pulses (black line). When $\tau \ll \theta$, the response is mainly viscous and deformations are essentially irreversible, with no recovery between pulses (light gray line). When $\tau \sim \theta$, the response is viscoelastic and a partial recovery is observed between pulses (gray line). To test this experimentally, we defined the irreversibility index I as the ratio between the irreversible part of the deformation and the maximal deformation (Figure 2B, left panel) and measured I as a function of the pulse duration θ (Figure 2B, boxplot). The resulting plot shows that shorter pulses indeed tend to produce more reversible deformations, whereas longer pulses tend to produce more irreversible deformations, a signature of dissipative mechanics.

Two terms contribute to the elongation rate \dot{I} in Equation 1. One scales with MyoII activity m , whereas the other scales with MyoII accumulation rate \dot{m} . For a given pulse, the maximum of \dot{m} precedes the maximum of m . Hence, a straightforward consequence of viscoelasticity is that the maximal rate of elongation should precede the maximum of MyoII activity (Figure 2C, left panel). We observed that this is indeed the case *in vivo* (Figure 2C, right panel). The model predicts a shift of about 25s between \dot{I} and m , which is consistent with our data. Indeed, we measured a shift of 29.5 ± 2 s for shortening (mean \pm SE) and 28.5 ± 2 s for elongation (Figure 2D). Whereas it was not interpreted in viscoelastic terms before, this shift was previously reported using temporal cross-correlation analysis during junction shortening [8], junction elongation [19], and prior to mesoderm invagination, when cells' apical area undergoes MyoII-driven contractions [5]. We interpret this consistent shift between MyoII activity and deformation rate as another signature of viscoelastic mechanics.

We have presented semiquantitative results showing that irreversible deformations generated by MyoII pulses bear the signature of viscoelastic dissipative mechanics. To assess more quantitatively the accuracy of the model, and hence to estimate the typical dissipation timescale, a direct comparison between experimental and model deformation dynamics is required. To that end, we extracted signals of MyoII activity from shortening and elongation movies (see, for example, Movie S1) and plugged them into our model. We then solved Equation 1 and predicted the resulting junction length dynamics $I(t)$. This prediction depends on the value of parameters κ_α and τ , which we use as adjustable parameters to obtain the best possible fit between the predicted and the experimental $I(t)$. The best fit is determined by iterating integration of Equation 1 using a gradient descent method. This analysis is per-

formed both for shortening events (Figure 2E, left panel) and elongation events (Figure 2E, right panel). Each fit yields an estimate of the timescale τ . We find a value of 61 ± 9 s for junction shortening (mean \pm SE) and a similar value of 56 ± 6 s for junction elongation (Figure 2F). Interestingly, this timescale is slightly shorter than the typical duration of MyoII pulses (typically 80 – 100s), which, according to the model, allows dissipation during the pulse and efficient junction shortening or elongation with little recovery (i.e., reversibility) between consecutive pulses.

Our analysis of MyoII pulses partly relies on the supposed scaling between MyoII activity and force generation. Therefore, we sought to confirm our mechanical analysis using better known forces, applied in a controlled fashion. In a previous study, we introduced optical tweezers as a tool to deform junctions in the embryonic epithelium of *Drosophila* and to study mechanics on short timescales. Here, we use similar optical forces to perform pull-release experiments on the minute timescale to study the irreversibility of deformations. Because of rapid cell movements occurring during germband elongation (stage 7), we could not perform the tweezers experiments at that stage. Therefore, we performed the experiments at stage 6, typically 15 min prior to the onset of elongation (see STAR Methods for details).

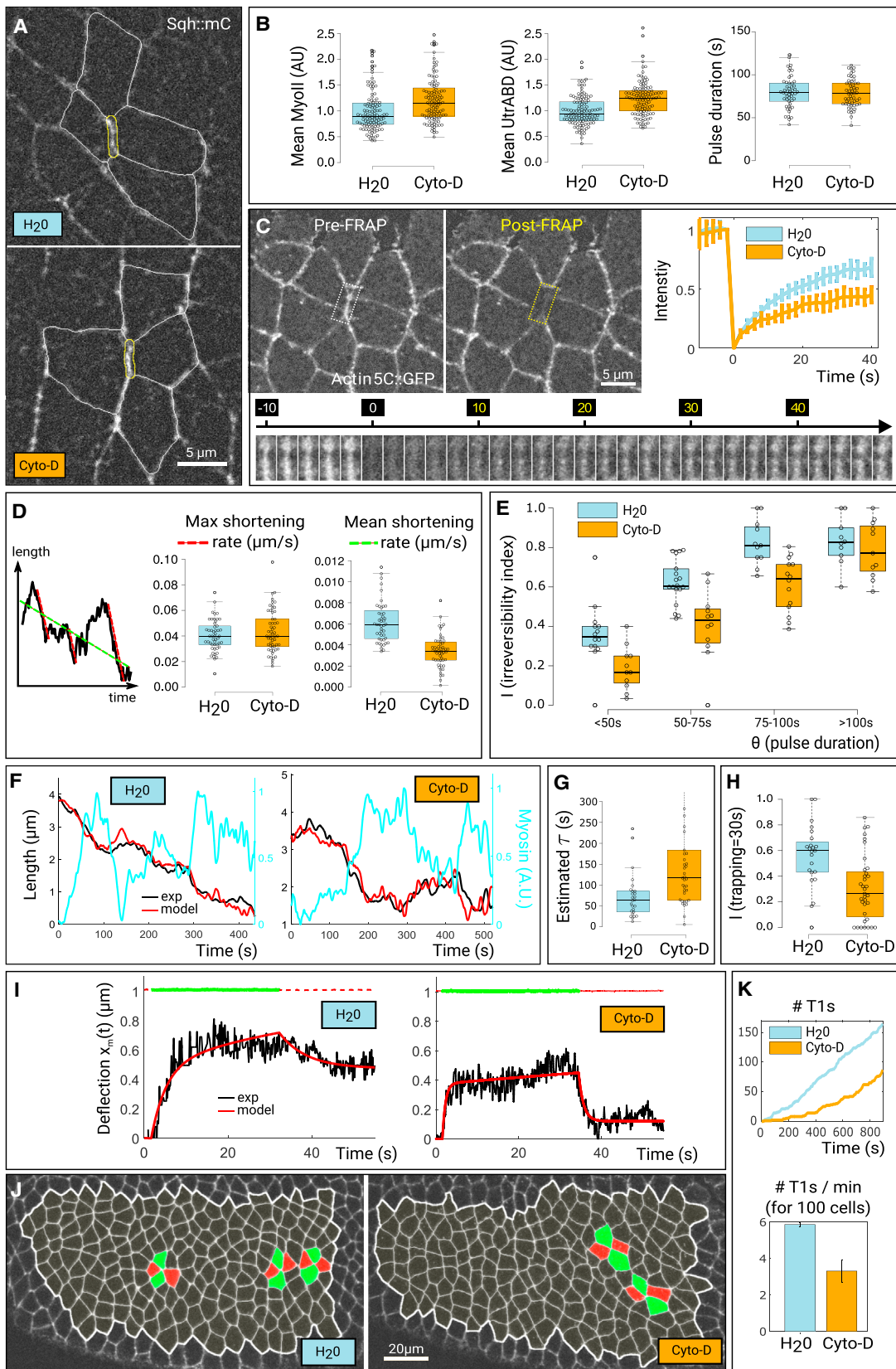
The trap is switched on at a distance x_t of a few hundred nanometers from the midpoint of a junction and then switched off after θ seconds (Figure 3A). We monitor the deflection $x_m(t)$ of the junction from its initial position, that is, $x_m(0) = 0$ (Figures 3B–3D; Movies S2, S3, and S4). Assuming a viscoelastic behavior with dissipation on timescale τ again yields a Maxwell-like constitutive equation relating the deflection $x_m(t)$ to the restoring force $f(t)$,

$$-k\ddot{x}_m = \dot{f} + \frac{f}{\tau}, \quad (\text{Equation 2})$$

where k is the effective elastic stiffness of the junction (see STAR Methods for details). Because the trap is instantly switched on or off, the junction undergoes rapid movements and the drag force in the cytosol $f_d = -C_\eta \dot{x}_m$, where C_η is the drag coefficient, can no longer be neglected. The trap force simply writes $f_t = k_t(x_t - x_m)$, where k_t is the optical trap stiffness [18]. Combining this constitutive equation to the force balance $f + f_t + f_d = 0$ yields the following equation of motion:

$$\ddot{x}_m + \left(\frac{1}{\tau} + \frac{1+\beta}{T} \right) \dot{x}_m + \frac{\beta}{\tau T} x_m = \frac{\beta}{\tau T} x_t. \quad (\text{Equation 3})$$

- (D) Kymographs of the deflection transverse to the junction, with $\theta = 5$ s (left panel), $\theta = 20$ s (middle panel), and $\theta = 40$ s (right panel). Green and red arrows indicate the trap being switched on and off. The scale bar for X represents 5 s and for Y represents 5 μ m.
- (E) Graphs of junction deflection extracted from kymographs, with $\theta = 3$ s (top panel) and $\theta = 40$ s (bottom panel). The solid black line shows the junction position $x_m(t)$. The horizontal line displays the optical trap position and its status (on, green; off, dotted red). The red line shows the fit obtained from our model.
- (F) Estimates of τ extracted from fits of experiments, both for optical tweezers ($n = 19$ from 6 embryos) and contractile pulses (shortening and extension; $n = 31$ from 6 embryos).
- (G) Left: Kymograph (top) and quantification (bottom, a.u.) of the MyoII signal during a trapping experiment. Green arrow indicates the initial deflection. Right: Boxplot of MyoII intensity at the onset of trapping versus after 40 s of trapping is shown ($n = 20$ from 5 embryos).
- (H) Left: Cartoon of the irreversibility index I , defined as the ratio between the irreversible deformation and the maximal deformation. Right: Irreversibility index $I(\theta)$ increases with the pulling time θ . Black dots show individual experiments ($n = 31$ from 6 embryos). The solid red line shows the analytical prediction, with no fit parameters.
- (I) Irreversibility index for $\theta = 30$ s as a function of the maximum amplitude of deflection, for controls ($n = 27$ from 8 embryos) and for embryos treated with cytochalasin-D ($n = 35$ from 11 embryos; see Figure 4 for Cyto-D experiments).



(legend on next page)

Note that inertia was neglected from the force balance because the system is at very low Reynolds number. [Equation 3](#) has three parameters. $\beta = k_t/k$ is dimensionless and compares the trap stiffness to the junction stiffness. It typically controls how far the junction elastically goes toward the optical trap. $\beta = 0$ when the trap is off; otherwise, our previous study showed that $\beta \sim 1$ [18]. $T = C_\eta/k$ is the timescale associated with viscous damping in the cytosol, i.e., the typical time required for the junction to elastically relax into and out of the trap. Our previous study showed that T is in the order of one to a few seconds [18]. Again, τ is the typical dissipation timescale and underlies the extent of irreversibility.

Consistent with our analysis of contractile pulses, we found that, if the duration of force application θ is long enough, irreversible deformations are observed. If θ is small, typically a few seconds, deformation is mostly reversible ([Figure 3E](#), top panel). For larger values of θ , deformations become more and more irreversible ([Figure 3E](#), bottom panel). In addition, we used the solution to [Equation 3](#) to fit the dynamics of junction deflection in and out of the trap ([Figure 3E](#)). Each fit provides an estimate of the three independent parameters β , T , and τ . Consistent with our previous estimates [18], we found that $\beta = 1.8 \pm 0.7$ and $T = 3 \pm 1$ s (mean \pm SE). More importantly, we obtained $\tau = 50 \pm 7$ s, which is in agreement with the estimates obtained from MyoII pulses analysis ([Figure 3F](#)). We next controlled whether the force applied by optical tweezers could trigger MyoII recruitment at junctions, as force application has been reported to promote MyoII recruitment to the cortex [25, 26]. Analyzing kymographs of MyoII signal ([Figure 3G](#), left panel), we measured no increase of MyoII during trapping experiments ([Figure 3G](#), right panel). This shows that stabilization is not due to MyoII recruitment induced by force application. Note that this is not contradictory with observations by Fernandez-Gonzalez et al. in *Drosophila* [26], because we apply weaker forces during a shorter period and at an earlier stage.

We observed that longer force application times yield deformations that are more irreversible. We thus defined the irreversibility index $I(\theta)$ as the ratio between the irreversible part of the deflection and the maximal deflection ([Figure 3H](#), left panel). From [Equation 3](#), it is possible to calculate analytically the irre-

versibility index as a function of the duration of force application θ (see [STAR Methods](#) for details). We measured $I(\theta)$ for θ ranging from 2 to 55 s (longer times were not experimentally accessible due to cell movements) and compared experimental measurements to the theoretical prediction ([Figure 3H](#), right panel). Note that this prediction has no adjustable parameters, because we directly used the values of β , T , and τ obtained earlier. Finally, we controlled whether irreversibility was not biased by the deflection amplitude, which might be larger for longer pulling experiments. To that end, we performed a series of experiments with a fixed pulling duration of $\theta = 30$ s. Variability of junction stiffness or trapping stiffness generated a significant variability in deflection amplitude. We found no correlation between the amplitude of deflection and the extent of irreversibility ([Figure 3I](#)). Overall, the good agreement between viscoelastic modeling and experiments further confirms our estimate of τ and the relevance of viscoelasticity to interpret junctional mechanics.

The molecular origin of dissipation at cell contacts is a complex issue. Turnover of the actomyosin cortex, believed to dissipate elastic energy stored in deformed actin filaments (F-actin) and of actin crosslinkers, might in part underlie irreversibility [22, 27]. In an attempt to investigate this question, we tested the possible role of F-actin turnover. We expect that increased F-actin stability, by slowing down adaptation of the cortex to cell shape changes, might reduce dissipation and therefore yield more reversible contractile events. To that end, we injected embryos with low dosage of cytochalasin D (Cyto-D), which is known in these conditions to reduce actin turnover by inhibiting both the polymerization and depolymerization of filaments barbed ends [28–30]. Importantly, treated embryos were still able to recruit MyoII at junctions and to undergo junction shortening ([Figure 4A](#); [Movie S5](#)). We also controlled that MyoII and F-actin (using the actin binding domain of Utrophin fused to GFP as a proxy for F-actin) intensities were commensurate with controls and that the typical duration of contractile events was similar ([Figure 4B](#)). As reported for melanoma M2 cells [30], experiments of fluorescence recovery after photo-bleaching (FRAP) in actin-GFP-expressing embryos confirmed that F-actin was more stable in embryos treated with low

Figure 4. Impact of Actin Dynamics on Dissipation

- (A) Junctions undergoing shortening (yellow area) in both water and Cyto-D-injected embryos. White lines evidence the segmentation of surrounding cells.
- (B) Averaged intensity of MyoII (left panel) and UtrophinABD (middle panel) at junctions in both water ($n = 115$ from 5 embryos) and Cyto-D embryos ($n = 112$ from 5 embryos). Right: Duration of contractile events in water ($n = 50$ from 3 embryos) and Cyto-D embryos ($n = 55$ from 3 embryos) is shown.
- (C) Pre- and post-FRAP images showing the loss of actin-GFP signal caused by photobleaching. (Bottom panel) Time-lapse sequence of the FRAP area is shown. Right: Recovery of the actin signal both in water (averaged from $n = 25$ junctions from 4 embryos) and Cyto-D embryos (averaged from $n = 25$ junctions from 8 embryos) is shown.
- (D) Left: Cartoon of the maximal shortening rate of a contractile event (red line) and of the averaged shortening rate (green line). Middle: Maximal shortening rate in water ($n = 50$ from 3 embryos) and Cyto-D embryos ($n = 57$ from 3 embryos) is shown. Right: Averaged shortening rate in water ($n = 47$ from 3 embryos) and Cyto-D embryos ($n = 52$ from 3 embryos) is shown.
- (E) Irreversibility index $I(\theta)$ of contractile events as a function of their duration both in water ($n = 51$ from 3 embryos) and Cyto-D embryos ($n = 48$ from 3 embryos).
- (F) Fit of junction shortening in both water (left panel) and Cyto-D embryos (right panel) using the experimental MyoII signal as input for the model.
- (G) Estimates of τ extracted from fits of shortening events for water ($n = 26$ from 3 embryos) and Cyto-D embryos ($n = 38$ from 3 embryos).
- (H) Irreversibility ratio after 30 s pulling with optical tweezers in both water ($n = 23$ from 8 embryos) and Cyto-D embryos ($n = 35$ from 11 embryos).
- (I) Sample kymographs of junction deflection in water and Cyto-D embryos.
- (J) Segmented view of the germband in water-injected and Cyto-D-injected embryos. T1 transitions extracted from [Movie S6](#) are depicted in green and red on the image.
- (K) Top: Cumulative sum of T1 transitions measured from [Movie S6](#). Bottom: Averaged frequency of T1 transitions for water ($n = 4$ embryos) and Cyto-D ($n = 4$ embryos) is shown. Error bars represent the SE.

concentrations of Cyto-D than in embryos injected with water (**Figure 4C**).

To assess the impact of Cyto-D on the dynamics of single junctions, we monitored MyoII activity and junction length during junction shortening. We first found that the maximal shortening rate during shortening events was similar in control and treated embryos, suggesting that the ability of MyoII to generate contractile forces and deform junctions was not affected (**Figure 4D**, middle panel). However, we found that the averaged shortening rate over longer periods, encompassing the contribution of several consecutive contractile events, was slower in embryos treated with Cyto-D (**Figure 4D**, right panel). This suggests that elastic recoil following shortening events is likely to be more important in treated embryos. This was confirmed by the quantification of the irreversibility index (as defined earlier), which we found consistently lower in embryos treated with Cyto-D (**Figure 4E**). We next used our viscoelastic model to fit the shortening dynamics in both control and treated embryos (**Figure 4F**). The good agreement obtained between predicted and observed shortening suggests that the treatment preserves the viscoelastic nature of the system while increasing the typical timescale of dissipation (**Figure 4G**). To further confirm this result, we went back to optical tweezers and performed a series of 30-s pulling experiments in both water and Cyto-D-injected embryos (**Figure 4I**). We then measured the irreversibility index and found that deformations in Cyto-D-treated embryos were on average almost twice as reversible than in the controls (**Figure 4H**).

Finally, we sought to determine whether the reduction of F-actin turnover had an impact on cell intercalation at the scale of the tissue, as could be expected from the increased reversibility of contractile events. To that end, we tracked cells by automated segmentation and counted the number of resolved T1 transitions during germband extension (**Figure 4J**; **Movie S6**). We found that Cyto-D treatment decreased the frequency of T1s (**Figure 4K**), consistent with recent reports showing that Cyto-D affects vertex resolution in this system [24] and suggesting that actin-dependent reversibility of contractile events affects intercalation.

The analysis of Cyto-D-treated embryos thus indicates that F-actin turnover participates in dissipation at cell contacts.

DISCUSSION

The analysis of irreversible cellular deformations resulting from both intrinsic and extrinsic forces reveals that dissipation at cell junctions occurs on the minute timescale in the germband of *Drosophila*. A direct consequence is that transient morphogenetic forces, such as those produced by pulsatile MyoII activity, can locally generate cell shape changes that are irreversible if they typically last a minute or more. This view is supported by our results showing that longer pulses, or longer tweezing, yield less reversible deformations. Unlike a purely elastic material, junctions submitted to increased forces due to increased MyoII activity dissipate elastic energy. This results in a drift of the reference configuration. Consequently, no or little elastic recoil is observed when MyoII activity drops down to its reference level after a pulse, because pulses typically span timescales commensurate with the timescale of dissipation. On the contrary, sudden removal of mechanical loading, for instance, by

laser ablation [23, 26] or rapid MyoII inhibition through Rok [31], still reveals the stress that was imposed prior to unloading and therefore yields elastic recoil. Indeed, dissipation of elastic energy does not imply that the system is devoid of mechanical stress, which in this case is continuously generated by MyoII. Dissipative mechanics thus provides a powerful explanation for the so-called mechanical ratchet, suggesting that the stabilization of active junction shortening or elongation might result from dissipation without the need of specific stabilizing forces.

It is important to note that the observed shortening or elongation of most junctions is quite far from the “canonical” dynamics with periodic pulses and stepwise deformations. Indeed, MyoII activity is usually far from being periodic, and its fluctuations are quite noisy. Interestingly, this is not a limiting factor for our mechanical interpretation, as the model is independent of the shape of MyoII signal. A consequence is that it provides no explanation as to why junctional remodeling occurs on a pulsatile basis. However, theoretical works have proposed generic mechanisms underlying the emergence of pulsatile contractility, either as resulting from the spontaneous instability of a turning-over material contracting against elastic elements [32] or from the advection and diffusion of two antagonistic species that up- and downregulate stress [33].

In this article, we sought to shed light on a series of biological observations with simple physical concepts rather than to develop a realistic description of the system’s rheology. As stated earlier, a consequence is that the viscoelastic model delineated here is an oversimplification, albeit a useful one, and is unlikely to reflect the complete rheological complexity of the system. Indeed, junctions and their cortex are likely to dissipate energy on a distribution of timescales and possibly involve non-linear viscoelasticity. Yet, our model is sufficient to quantitatively interpret the *in vivo* data accessible to our experiments. More precise rheological measurements would be necessary to develop more sophisticated rheological models. This remains experimentally challenging, especially *in vivo*.

At the tissue scale, morphogenetic deformations are likely to involve a variety of additional contributors. It was recently shown that a subset of rosette formation events, which are not considered in this study, result from basolateral protrusive activity [34] rather than from apical MyoII contractility. This suggests that other mechanisms of cell deformations might be at play, presumably involving different mechanical interactions. Similarly, possible friction with the yolk and vitelline membrane are not considered here, nor topological transitions between cells. The formation of new antero-posterior junctions, because they modify tissue topology, might, for instance, be required for long-term stabilization of large, tissue-scale elongation once MyoII polarity is lost. Such contributions are likely to involve effective dissipation timescales at the tissue scale, possibly larger than a minute, as suggested by recent rheological measurements performed using ferrofluid droplets [35]. Note that, in suspended monolayers, which display no or very few topological transitions and have no substrate, stress relaxation at the tissue scale typically occurs on the minute timescale [17], consistent with our estimate. Although this is out of the scope of this study, continuum mechanics models might provide a more adequate framework to describe the full tissue dynamics [36, 37]. Bridging the gap between subcellular analysis, such as ours, and macroscopic models of tissue flows, which can incorporate effective

mechanical parameters as well as a wide variety of cell behaviors (topological transitions, growth, division, apoptosis, etc.), remains a challenge for the physics of tissue morphogenesis.

The question as to how elastic energy is dissipated at the molecular level remains rather open. A common view is that most of the elastic energy is stored by deformed actin filaments and actin crosslinkers and that their turnover is therefore likely to dissipate elastic energy [9, 27]. In that scenario, newly created filaments are indeed devoid of the elastic energy stored by the previous ones, and the turnover rate critically affects the dissipation timescale. This view is supported by theoretical models [38] and by our Cyto-D experiments (Figure 4). We anticipate that further work will be required to investigate other possible molecular sources of dissipation. MyoII in particular has, for instance, been shown to fluidize the cytoskeletal network [39, 40] and enhance actin disassembly [41]. Irrespective of its contractile activity, MyoII is also likely to contribute to dissipation as a turning-over crosslinker of the cortical network. Anchorage of the actomyosin network to junctions, suggested to be affected by actin turnover inhibition [42], might affect cell shape changes [43] and possibly irreversibility. The redistribution of adhesion molecules at deformed junctions might also be important to stabilize deformations, and the rate of E-cadherin complex disassembly (e.g., via endocytosis) might thus be a limiting factor for stabilization. Interestingly, such contributions of protein dynamics to dissipation allow cell-, tissue-, or organ-specific regulation of the dissipation timescales. This offers a versatile tool for morphogenesis: besides the ability of cells to generate localized and/or polarized forces, local and/or polarized control of the mechanical response to forces become possible, not only in a quantitative manner (stiffer or softer), but in a qualitative manner (more elastic or more viscous). Tissue-specific tuning of dissipative properties might also be important to ensure that short-lived mechanical stresses do not produce dramatic irreversible deformations. In the system investigated here, the timescale of force generation, that is, the timescale of MyoII pulses, is commensurate with the typical dissipation timescale, which seems crucial to achieve efficient deformations. This observation might be relevant to other morphogenetic systems, although further work will be required to confirm this hypothesis. In particular, other morphogenetic events displaying reversible and irreversible contractions should be analyzed. For example, actomyosin pulses during zebrafish optic cup morphogenesis drive essentially reversible shortening events of cells' apico-basal axis length [44]. Interestingly and in contrast with cells investigated here, shortening and MyoII oscillations seem synchronous, which is consistent with a reversible, elastic regime of deformation. Similarly, during the first phase of dorsal closure, pulses of MyoII in the medio-apical cortex cause reversible contractions of amniotic cells' apical area [45, 46]. This is followed by a second phase, during which contractile events become more efficient, with net shrinkage after each pulse. A possible mechanism is a gradual increase of dissipation during the process, causing pulses to first probe an elastic regime, whereas, as time passes, they probe an increasingly viscous regime, allowing more efficient deformations.

Altogether, our results provide an *in vivo* estimate of the typical dissipation timescale associated with junctional remodeling and shed a new light on the mechanism of the so-called mechanical ratchet, highlighting the key contribution of dissipation in stabilizing deformations. It opens a new avenue for the understanding

of tissue morphogenesis and the irreversibility of deformations by an emphasis on viscoelastic, dissipative properties of cells beyond force generation per se.

STAR★METHODS

Detailed methods are provided in the online version of this paper and include the following:

- KEY RESOURCES TABLE
- CONTACT FOR REAGENTS AND RESOURCE SHARING
- EXPERIMENTAL MODEL AND SUBJECT DETAILS
- METHOD DETAILS
 - Imaging and quantification of MyoII pulses
 - Optical tweezers
 - Cytochalasin-D injections
 - Fluorescence recovery after photobleaching
 - Quantifications of T1 transitions
 - Model – MyoII pulses
 - Model – optical tweezers
- QUANTIFICATION AND STATISTICAL ANALYSES
- DATA AND SOFTWARE AVAILABILITY

SUPPLEMENTAL INFORMATION

Supplemental Information includes six movies and can be found with this article online at <http://dx.doi.org/10.1016/j.cub.2017.09.005>.

AUTHOR CONTRIBUTIONS

R.C. and P.-F.L. conceived the project and discussed it with C.C. and T.L. B.D. and C.C. performed the myosin pulses experiments (Figure 2), and B.D., C.C., and R.C. analyzed the data. R.C. performed the optical tweezers experiments (Figures 3 and 4) and analyzed the data. B.D. performed the Cyto-D experiments (Figure 4), and B.D. and R.C. analyzed the data. R.C. designed the model. All authors discussed the results. R.C. wrote the manuscript, and all authors commented on it.

ACKNOWLEDGMENTS

We thank Claire Chardès for assistance with the optical tweezers setup and members of the Lenne and Lecuit groups for stimulating and useful discussions during the course of this project. This work was supported by an FRM Equipe Grant FRM DEQ20130326509, Agence Nationale de la Recherche ANR-Blanc Grant Morfor ANR-11-BSV5-0008 (to P.-F.L.), the ERC Grant BioMecaMorph (to T.L.), and LabEx INFORM (ANR-11-LABX-0054) of the A*MIDEX project (ANR-11-IDEX-0001-02), funded by the French Government program “Investissements d'Avenir”. We acknowledge France-BioImaging infrastructure supported by the Agence Nationale de la Recherche (ANR-10-INBS-04-01; “Investissements d'Avenir”). B.D. was supported by the ERC Grant BioMecaMorph (323027), and C.C. was supported by a Human Frontier Science Program Long-Term Fellowship (LT000733/2011-L) and by a postdoctoral fellowship from the FRM (SPF20121226396).

Received: May 11, 2017

Revised: July 27, 2017

Accepted: September 5, 2017

Published: October 5, 2017

REFERENCES

1. Lecuit, T., Lenne, P.-F., and Munro, E. (2011). Force generation, transmission, and integration during cell and tissue morphogenesis. *Annu. Rev. Cell Dev. Biol.* 27, 157–184.

2. Heisenberg, C.P., and Bellaïche, Y. (2013). Forces in tissue morphogenesis and patterning. *Cell* 153, 948–962.
3. Bertet, C., Sulak, L., and Lecuit, T. (2004). Myosin-dependent junction remodelling controls planar cell intercalation and axis elongation. *Nature* 429, 667–671.
4. Blankenship, J.T., Backovic, S.T., Sanny, J.S., Weitz, O., and Zallen, J.A. (2006). Multicellular rosette formation links planar cell polarity to tissue morphogenesis. *Dev. Cell* 11, 459–470.
5. Martin, A.C., Kaschube, M., and Wieschaus, E.F. (2009). Pulsed contractions of an actin-myosin network drive apical constriction. *Nature* 457, 495–499.
6. Munro, E., Nance, J., and Priess, J.R. (2004). Cortical flows powered by asymmetrical contraction transport PAR proteins to establish and maintain anterior-posterior polarity in the early *C. elegans* embryo. *Dev. Cell* 7, 413–424.
7. Skoglund, P., Rolo, A., Chen, X., Gumbiner, B.M., and Keller, R. (2008). Convergence and extension at gastrulation require a myosin IIB-dependent cortical actin network. *Development* 135, 2435–2444.
8. Rauzi, M., Lenne, P.-F., and Lecuit, T. (2010). Planar polarized actomyosin contractile flows control epithelial junction remodelling. *Nature* 468, 1110–1114.
9. Wyatt, T., Baum, B., and Charras, G. (2016). A question of time: tissue adaptation to mechanical forces. *Curr. Opin. Cell Biol.* 38, 68–73.
10. He, B., Doubrovinski, K., Polyakov, O., and Wieschaus, E. (2014). Apical constriction drives tissue-scale hydrodynamic flow to mediate cell elongation. *Nature* 508, 392–396.
11. Dicko, M., Saramito, P., Blanchard, G.B., Lye, C.M., Sanson, B., and Étienne, J. (2017). Geometry can provide long-range mechanical guidance for embryogenesis. *PLoS Comput. Biol.* 13, e1005443.
12. Forgacs, G., Foty, R.A., Shafir, Y., and Steinberg, M.S. (1998). Viscoelastic properties of living embryonic tissues: a quantitative study. *Biophys. J.* 74, 2227–2234.
13. Desprat, N., Richert, A., Simeon, J., and Asnacios, A. (2005). Creep function of a single living cell. *Biophys. J.* 88, 2224–2233.
14. Plotnikov, S.V., Sabass, B., Schwarz, U.S., and Waterman, C.M. (2014). High-resolution traction force microscopy. *Methods Cell Biol.* 123, 367–394.
15. Bufl, N., Durand-Smet, P., and Asnacios, A. (2015). Single-cell mechanics: the parallel plates technique. *Methods Cell Biol.* 125, 187–209.
16. Harris, A.R., Bellis, J., Khalilgharibi, N., Wyatt, T., Baum, B., Kabla, A.J., and Charras, G.T. (2013). Generating suspended cell monolayers for mechanobiological studies. *Nat. Protoc.* 8, 2516–2530.
17. Wyatt, T.P.J., Harris, A.R., Lam, M., Cheng, Q., Bellis, J., Dimitracopoulos, A., Kabla, A.J., Charras, G.T., and Baum, B. (2015). Emergence of homeostatic epithelial packing and stress dissipation through divisions oriented along the long cell axis. *Proc. Natl. Acad. Sci. USA* 112, 5726–5731.
18. Bambardekar, K., Clément, R., Blanc, O., Chardès, C., and Lenne, P.-F. (2015). Direct laser manipulation reveals the mechanics of cell contacts *in vivo*. *Proc. Natl. Acad. Sci. USA* 112, 1416–1421.
19. Collinet, C., Rauzi, M., Lenne, P.F., and Lecuit, T. (2015). Local and tissue-scale forces drive oriented junction growth during tissue extension. *Nat. Cell Biol.* 17, 1247–1258.
20. Munjal, A., Philippe, J.-M., Munro, E., and Lecuit, T. (2015). A self-organized biomechanical network drives shape changes during tissue morphogenesis. *Nature* 524, 351–355.
21. Kerridge, S., Munjal, A., Philippe, J.-M., Jha, A., de las Bayonas, A.G., Saurin, A.J., and Lecuit, T. (2016). Modular activation of Rho1 by GPCR signalling imparts polarized myosin II activation during morphogenesis. *Nat. Cell Biol.* 18, 261–270.
22. Blanchoin, L., Boujemaa-Paterski, R., Sykes, C., and Plastino, J. (2014). Actin dynamics, architecture, and mechanics in cell motility. *Physiol. Rev.* 94, 235–263.
23. Rauzi, M., Verant, P., Lecuit, T., and Lenne, P.-F. (2008). Nature and anisotropy of cortical forces orienting *Drosophila* tissue morphogenesis. *Nat. Cell Biol.* 10, 1401–1410.
24. Yu, J.C., and Fernandez-Gonzalez, R. (2016). Local mechanical forces promote polarized junctional assembly and axis elongation in *Drosophila*. *eLife* 5, e10757.
25. Effler, J.C., Kee, Y.S., Berk, J.M., Tran, M.N., Iglesias, P.A., and Robinson, D.N. (2006). Mitosis-specific mechanosensing and contractile-protein redistribution control cell shape. *Curr. Biol.* 16, 1962–1967.
26. Fernandez-Gonzalez, R., Simoes, S. de M., Röper, J.C., Eaton, S., and Zallen, J.A. (2009). Myosin II dynamics are regulated by tension in intercalating cells. *Dev. Cell* 17, 736–743.
27. Salbreux, G., Charras, G., and Paluch, E. (2012). Actin cortex mechanics and cellular morphogenesis. *Trends Cell Biol.* 22, 536–545.
28. Cooper, J.A. (1987). Effects of cytochalasin and phalloidin on actin. *J. Cell Biol.* 105, 1473–1478.
29. Shoji, K., Ohashi, K., Sampei, K., Oikawa, M., and Mizuno, K. (2012). Cytochalasin D acts as an inhibitor of the actin-cofilin interaction. *Biochem. Biophys. Res. Commun.* 424, 52–57.
30. Fritzsche, M., Lewalle, A., Duke, T., Kruse, K., and Charras, G. (2013). Analysis of turnover dynamics of the submembranous actin cortex. *Mol. Biol. Cell* 24, 757–767.
31. Coravos, J.S., and Martin, A.C. (2016). Apical sarcomere-like actomyosin contracts nonmuscle *Drosophila* epithelial cells. *Dev. Cell* 39, 346–358.
32. Dierkes, K., Sumi, A., Solon, J., and Salbreux, G. (2014). Spontaneous oscillations of elastic contractile materials with turnover. *Phys. Rev. Lett.* 113, 148102.
33. Kumar, K.V., Bois, J.S., Jülicher, F., and Grill, S.W. (2014). Pulsatory patterns in active fluids. *Phys. Rev. Lett.* 112, 208101.
34. Sun, Z., Amourda, C., Shagirov, M., Hara, Y., Saunders, T.E., and Toyama, Y. (2017). Basolateral protrusion and apical contraction cooperatively drive *Drosophila* germ-band extension. *Nat. Cell Biol.* 19, 375–383.
35. Doubrovinski, K., Swan, M., Polyakov, O., and Wieschaus, E.F. (2017). Measurement of cortical elasticity in *Drosophila melanogaster* embryos using ferrofluids. *Proc. Natl. Acad. Sci. USA* 114, 1051–1056.
36. Prost, J., Jülicher, F., and Joanny, J.-F. (2015). Active gel physics. *Nat. Phys.* 11, 111–117.
37. Tlili, S., Gay, C., Graner, F., Marcq, P., Molino, F., and Saramito, P. (2015). Colloquium: mechanical formalisms for tissue dynamics. *Eur. Phys. J. E* 38, 33–63.
38. Kim, T., Gardel, M.L., and Munro, E. (2014). Determinants of fluidlike behavior and effective viscosity in cross-linked actin networks. *Biophys. J.* 106, 526–534.
39. Le Goff, L., Amblard, F., and Furst, E.M. (2002). Motor-driven dynamics in actin-myosin networks. *Phys. Rev. Lett.* 88, 018101.
40. Humphrey, D., Duggan, C., Saha, D., Smith, D., and Käs, J. (2002). Active fluidization of polymer networks through molecular motors. *Nature* 416, 413–416.
41. Wilson, C.A., Tsuchida, M.A., Allen, G.M., Barnhart, E.L., Applegate, K.T., Yam, P.T., Ji, L., Keren, K., Danuser, G., and Theriot, J.A. (2010). Myosin II contributes to cell-scale actin network treadmilling through network disassembly. *Nature* 465, 373–377.
42. Jodoi, J.N., Coravos, J.S., Chanet, S., Vasquez, C.G., Tworoger, M., Kingston, E.R., Perkins, L.A., Perrimon, N., and Martin, A.C. (2015). Stable force balance between epithelial cells arises from F-actin turnover. *Dev. Cell* 35, 685–697.
43. Roh-Johnson, M., Shemer, G., Higgins, C.D., McClellan, J.H., Werts, A.D., Tulu, U.S., Gao, L., Betzig, E., Kiehart, D.P., and Goldstein, B. (2012). Triggering a cell shape change by exploiting preexisting actomyosin contractions. *Science* 335, 1232–1235.

44. Nicolás-Pérez, M., Kuchling, F., Letelier, J., Polvillo, R., Wittbrodt, J., and Martínez-Morales, J.R. (2016). Analysis of cellular behavior and cytoskeletal dynamics reveal a constriction mechanism driving optic cup morphogenesis. *eLife* 5, 1–24.
45. Solon, J., Kaya-Çopur, A., Colombelli, J., and Brunner, D. (2009). Pulsed forces timed by a ratchet-like mechanism drive directed tissue movement during dorsal closure. *Cell* 137, 1331–1342.
46. Machado, P.F., Duque, J., Étienne, J., Martinez-Arias, A., Blanchard, G.B., and Gorfinkiel, N. (2015). Emergent material properties of developing epithelial tissues. *BMC Biol.* 13, 98.
47. Guillot, C., and Lecuit, T. (2013). Adhesion disengagement uncouples intrinsic and extrinsic forces to drive cytokinesis in epithelial tissues. *Dev. Cell* 24, 227–241.
48. Aigouy, B., Farhadifar, R., Staple, D.B., Sagner, A., Röper, J.C., Jülicher, F., and Eaton, S. (2010). Cell flow reorients the axis of planar polarity in the wing epithelium of *Drosophila*. *Cell* 142, 773–786.
49. Cavey, M., and Lecuit, T. (2008). Imaging cellular and molecular dynamics in live embryos using fluorescent proteins. *Methods Mol. Biol.* 420, 219–238.
50. Spitzer, M., Wildenhain, J., Rappaport, J., and Tyers, M. (2014). BoxPlotR: a web tool for generation of box plots. *Nat. Methods* 11, 121–122.

STAR★METHODS

KEY RESOURCES TABLE

REAGENT or RESOURCE	SOURCE	IDENTIFIER
Chemicals, Peptides, and Recombinant Proteins		
Cytochalasin D	Sigma	C8273
Deposited Data		
Mendeley dataset	This paper	http://dx.doi.org/10.17632/my2dcbrf8g.1
Experimental Models: Organisms/Strains		
<i>D. melanogaster</i> / ; Sqh::GFP; Gap43::mCherry	[47]	N/A
<i>D. melanogaster</i> / ; E-cad::GFP, Sqh::mCherry;	[47]	N/A
<i>D. melanogaster</i> / ; GFP::UtrophinABD, Sqh::mCherry	This paper	N/A
<i>D. melanogaster</i> / ; UAS-GFP::Actin5C ;	Bloomington Drosophila Stock Center	9258
Software and Algorithms		
Tissue Analyzer	[48]	https://grr.gred-clermont.fr/labmirouse/software/WebPA/index.html
Other		
Invitrogen FluoSpheres carboxylate-modifies 0.5μm red fluorescent	Thermo Fisher	F8812

CONTACT FOR REAGENTS AND RESOURCE SHARING

Further information and requests for resources and reagents should be directed to and will be fulfilled by the Lead Contact, Raphaël Clément (raphael.clement@univ-amu.fr).

EXPERIMENTAL MODEL AND SUBJECT DETAILS

Flies were maintained under standard lab conditions at 22°C with yeast food. In order to obtain embryos, flies were put in standard cages. Cages feature an agar plate with apple juice at the bottom, supplemented with fresh yeast paste. Flies lay eggs on these plates. To collect embryos we filtered the yeast paste supplemented with H₂O. Embryos are covered by a non-transparent chorion which needs to be removed for live imaging. To do so we treated the embryos with commercial bleach for 45 s, and then washed them abundantly with H₂O. Embryos were then staged and aligned on coverslips using binoculars. Coverslips were then taken to fluorescence microscopes for live imaging. For more details about embryo preparation, see [49]. Please refer to method details for strains used for each experiment.

METHOD DETAILS

Imaging and quantification of MyoII pulses

Fly embryos were imaged during germband elongation (stage 7) in the ventro-lateral region for about 30 min. For Figures 1 and 2, embryos labeled with E-cadherin::GFP (*shg* in *Drosophila*) and MyoII regulatory light chain (MRLC)::mCherry (*sqh* in *Drosophila*) were from a fly stock sqhAX3; E-cad::GFPKIn, sqh-Sqh::mCherry. For Figure 4, embryos labeled with GFP::UtrophinABD and Sqh::mCherry were used. The fly line ; ; GFP::UtrophinABD, Sqh::mCherry was generated using a sqh-GFP::UtrophinABD transgene [8] recombined with the sqh-Sqh::mCherry transgene [5], both inserted on the third chromosome.

Time-lapse imaging was performed with a spinning disk confocal microscope (Eclipse TE 2000-E with an Ultraview ERS, Perkin Elmer spinning disk) using a 100X/N.A. 1.4 oil-immersion objective. Z series of 6–10 planes spanning 4–6 μm from the cell apex were acquired with a frame rate of 3 to 4.5 s/frame to collect both the medio-apical and the junctional MyoII pools. Maximum projections of confocal Z stack were generated for the image analysis, and cytoplasmic background was subtracted as previously described [19].

MyoII signal at the junctions was measured by measuring the mean fluorescence intensity of the MyoII channel in a 0.8 μm wide straight line connecting the junction vertices (Figure 1H). Fluorescence intensity at the vertices was excluded by shrinking the line of 5 pixel (0.4 μm) at both ends.

MyoII signal close to adjacent vertices was measured in adjacent anterior and posterior cells as the mean fluorescence intensity of the MyoII channel in two elliptical regions of interest (ROIs) close to the junction vertices. Ellipses have an aspect ratio of 0.7 and a major axis of 3 μm aligned along the line of the junction (Figure 1).

Optical tweezers

For optical tweezers experiments, fly embryos double-labeled with GFP::UtrophinABD and Sqh::mCherry were used, except Figure 3G, for which flies labeled with Sqh::GFP and Gap43::mCherry were used. Tweezers experiments were performed typically 15 min before germband elongation (stage 6). Rapid cell movements occurring throughout the extension process (stage 7) prevent “long” trapping experiments (more than 10–20 s). At stage 6 the tissue is static enough to allow longer trapping, although one-minute-long pulling experiments are already an upper limit considering cell movements. Imaging was done in a custom light sheet microscope coupled with a single-beam gradient trap (wavelength 1070 nm, ytterbium fiber laser; IPG photonics). A 100X water immersion lens (N.A. 1.1, Nikon) was used for imaging as well as introducing the optical trap in the imaging plane. Before every experiment, we calibrated the relationship between the galvanometers voltages (V_1, V_2) and the optical trap position (x, y), using the following procedure: 500 nm-diameter fluorescent polystyrene beads were trapped in water and moved slowly in circles by imposing galvanometers voltages. Images were acquired simultaneously to voltage commands, and successive (x, y) positions were localized by 2D Gaussian fits, providing the mapping between (V_1, V_2) and (x, y). This information was used to infer the trap position during in vivo experiments.

Kymographs of interface deflection were produced from movies using Fiji, and analyzed with a custom MATLAB script described below. Note that we neglected possible Z displacements likely to be caused by radiation pressure, which in a few experiments can move junctions slightly off focus while the trap is on (see for instance Figure 3D, right panel). To obtain the position of the cell-cell interface in the XY plane, the custom script performs a Gaussian fit of the fluorescence intensity of UtrophinABD or Gap43 along the kymograph line, perpendicular to the contact line. This is repeated for each frame, and allows subpixel detection of the deflection $x_m(t)$, with an error < 100 nm [18].

Cytchalasin-D injections

For injections experiments shown Figure 4, Cyto-D suspended in DMSO at a concentration of 10 $\mu\text{g}/\mu\text{l}$ was diluted 20 times in water, and injected in the yolk at the onset of gastrulation (stage 5–6). The final dilution factor in the embryo is around 1/50, so that we expect a final concentration of approximately 0.01 $\mu\text{g}/\mu\text{l}$. Water supplemented with the same quantity of DMSO (1/20) was injected for control experiments.

Fluorescence recovery after photobleaching

For FRAP experiments, F2 progeny of females ; 67Gal4 ; crossed with males ; UAS-GFP::Actin5C ; were used. Photobleaching was performed using the targeted laser of the Nikon Eclipse Ti spinning disc (iLAS2). A circular junctional region of typically 2.5 μm diameter was photobleached. Laser power and integration settings were adjusted to photobleach up to 80% of the initial intensity. The photo-bleached region was tracked using a custom macro in ImageJ. The fluorescence intensity of the photo-bleached region was measured at each time point, and normalized as $I_{\text{norm}} = (I - I_{\min}) / (I_{\max} - I_{\min})$ (Figure 4C).

Quantifications of T1 transitions

To measure the number of T1 transitions (Figures 4J and 4K), we used the Tissue Analyzer plugin for ImageJ developed by Benoît Aigouy [48]. Segmentation was automatically performed by the plugin and corrected by the experimenter. T1 events were automatically detected by the plugin and then checked individually by the experimenter to prevent false detections.

Model – MyoII pulses

Let us first consider an elastic cell-cell junction with modulus κ submitted to an elongation/shortening force f . The length of the junction is given by:

$$l = l_0 + \frac{f}{\kappa} \quad \text{Eq. 4}$$

Now let us assume that the reference configuration l_0 drifts due to dissipation. Since the system has a number of dissipation sources, possibly including the turnover of Actin and its many crosslinkers, it is likely to dissipate energy on a distribution of timescales. For the sake of simplicity we will assume that it dissipates energy on a single typical timescale τ and therefore that the reference configuration accordingly drifts over timescale τ . We thus have:

$$\dot{l}_0 = \frac{l - l_0}{\tau}. \quad \text{Eq. 5}$$

Dots denote time derivatives. Derivating Equation 4 with respect to time, using that $\dot{l}_0 = (l - l_0)/\tau = f/(\kappa\tau)$, and multiplying by κ yields the well-known Maxwell model of viscoelasticity:

$$\kappa\ddot{l} = \dot{f} + \frac{f}{\tau}. \quad \text{Eq. 6}$$

We now need to relate the force f to MyoII activity. We assume that f results from a balance between MyoII at the junction which tends to shorten junctions (minus sign), and MyoII in the vicinity of the junction vertices (and possibly in the neighboring junctions), which tend to elongate it (plus sign), so that $f = -f_j + f_v$. Note that with this convention both f_j and f_v are positive.

Let us first consider shortening events, powered by pulses of MyoII at junctions (M_j). We assume that the shortening force is proportional to MyoII level, so that $f_j = \alpha M_j$. During these events, MyoII in the vicinity of vertices (M_v) is low and does not display coherent fluctuations. Hence we assume that the opposing external force f_v is constant, so that $f_v = f_v^0$. Thus we have $f = -\alpha M_j + f_v^0$.

At rest (in the absence of pulses), the length l is constant and $f = 0$, and MyoII at the junction M_j is at a base level M_j^0 . Hence $-\alpha M_j^0 + f_v^0 = 0$, so that $f_v^0 = -\alpha M_j^0$. Therefore during shortening, f can be approximated as $f = -\alpha(M_j - M_j^0)$. One can interpret the base level M_j^0 as the amount of MyoII required at the junction to withstand the “constant” external force f_v^0 exerted by neighboring cells. Only the excess of MyoII compared to that base level will be able to shorten the junction. Practically, we assume that M_j^0 is the minimum of M_j , which is consistent with shortening junctions being at rest in the absence of pulses at the junction. Defining $m = M_j - M_j^0$, and $\kappa_\alpha = \kappa/\alpha$, we obtain for shortening:

$$-\kappa_\alpha \dot{l} = \dot{m} + \frac{m}{\tau}. \quad \text{Eq. 7}$$

Let us now consider elongation events, powered by pulses of MyoII in the vicinity of vertices (M_v). We assume that the elongation force is proportional to M_v , so that $f_v = \alpha M_v$. During elongation events, MyoII at the junction (M_j) is low and does not display coherent fluctuations. Hence in that case we assume that f_j is constant, so that $f_j = f_j^0$. With similar arguments on equilibrium, we obtain that $f_j^0 = \alpha M_v^0$, so that $f = +\alpha(M_v - M_v^0)$. M_v^0 is the base level of MyoII at vertices, and corresponds to the level of MyoII required to withstand the “constant” junction tension f_j^0 . Again, practically we assume that M_v^0 is the minimum of M_v , consistent with elongating junctions being at rest in the absence of pulses in the vicinity of vertices. Again, defining $m = M_v - M_v^0$, and $\kappa_\alpha = \kappa/\alpha$, we obtain for elongation:

$$+\kappa_\alpha \dot{l} = \dot{m} + \frac{m}{\tau}. \quad \text{Eq. 8}$$

[Equations 7](#) and [8](#) have two parameters. κ_α tells us to which extent MyoII can deform junctions, and hence contains both the elastic modulus of the cortex and the conversion constant from MyoII to force. τ is the typical dissipation timescale. Note that since MyoII pulses are slow compared to the timescale associated to viscous drag in the cytosol (one to a few seconds [18]), we neglected drag in the context of MyoII pulses.

To generate artificial data of shortening during pulses, we integrated [Equations 7](#) and [8](#) using Gaussian pulses of MyoII activity as input for m . To fit experimental data and estimate τ , we integrated [Equations 7](#) and [8](#) using the experimental MyoII signals as input for m . For each fit, the integration was iterated using a gradient descent method to obtain the best fit values for κ_α and τ . Note that MyoII intensity being in arbitrary units, κ_α also has arbitrary units.

Model – optical tweezers

Let us now consider a cell-cell junction submitted to an external normal force exerted by optical tweezers. The contact line is deflected from the straight reference configuration with an angle φ , hence the restoring force f is:

$$f = -2T \sin \varphi \quad \text{Eq. 9}$$

where T is the tension in the junction. For small deflection angles, $\sin \varphi \approx 2x_m/h$, where h is the junction length, x_m the deflection, and $T = T_0 = \text{cst}$ [18]. Hence,

$$f = -\frac{4T_0}{h}(x_m - x_0) = -k(x_m - x_0) \quad \text{Eq. 10}$$

where $k = 4T_0/h$ is the effective stiffness of the junction in response to perpendicular deflection, and x_0 the abscissa of the junction in the absence of trapping, with $x_0(t=0)=0$. Again, let us now assume that the reference configuration drifts on a typical timescale τ due to dissipation:

$$\dot{x}_0 = \frac{x_m - x_0}{\tau}. \quad \text{Eq. 11}$$

Combining [Equations 10](#) and [11](#) again yields a Maxwell-like viscoelastic equation:

$$-k\dot{x}_m = \dot{f} + \frac{f}{\tau}. \quad \text{Eq. 12}$$

The restoring force f is balanced by viscous drag in the cytosol and by optical trapping, which we can assume is linear [18]. Note that since we switch the trap rapidly from on/off to off/on, junctions are submitted to rapid movements, and unlike the case of MyoII pulses, here drag cannot be neglected. Finally we neglect the inertial term, since the system is at very low Reynolds number. The force balance reads:

$$f + k_t(x_t - x_m) - C_\eta \dot{x}_m = 0 \quad \text{Eq. 13}$$

where k_t is the stiffness of the optical trap, and C_η the damping coefficient due to drag in the cytosol. Combining [Equations 12](#) and [13](#) yields the equation of motion for the junction submitted to trapping:

$$\ddot{x}_m + \left(\frac{1}{\tau} + \frac{1+\beta}{T}\right)\dot{x}_m + \frac{\beta}{\tau T}x_m = \frac{\beta}{\tau T}x_t. \quad \text{Eq. 14}$$

This equation has three parameters. $\beta = k_t/k$ is the dimensionless ratio between the trap stiffness and the junction stiffness. Note that $\beta = 0$ if the trap is off. Otherwise $\beta \sim 1$ [18]. $T = C_\eta/k$ is the relaxation timescale associated to drag in the cytosol. In practice, we have $T \sim 3$ s. Finally τ is the timescale of dissipation, which we are primarily interested in.

Let us now introduce a and b such that $a = 1/\tau + (1 + \beta)/T$ and $b = \beta/\tau T$. [Equation 14](#) now reads:

$$\ddot{x}_m + a\dot{x}_m + bx_m = bx_t. \quad \text{Eq. 15}$$

Let Δ be the discriminant of the characteristic polynomial associated to [Equation 15](#), that is $\Delta = a^2 - 4b$. Using that x_t is a particular solution, the general solution to [Equation 15](#) reads:

$$x_m(t) = x_t(1 + Ae^{-t/\tau_A} + Be^{-t/\tau_B}) \quad \text{Eq. 16}$$

where $\tau_A = 2/(a + \Delta^{1/2})$ and $\tau_B = 2/(a - \Delta^{1/2})$. The first initial condition is: $x_m(t=0) = 0$. In addition, at the onset of deflection ($t=0^+$), the force balance reads: $C_\eta \dot{x}_m(t=0) = k_t x_t$, hence $\dot{x}_m(t=0) = k_t x_t / C_\eta$. Plugging these conditions in [Equation 16](#) yields the constants A and B . We find that $A = \tau_A(T - \beta\tau_B)/(T(\tau_B - \tau_A))$ and that $B = \tau_B(\beta\tau_A - T)/(T(\tau_B - \tau_A))$. We use [Equation 16](#) to fit pull-release experiments and to estimate the three parameters of the model β , T , and τ .

Let us now consider the relaxation process after a pulling experiment of duration θ (hence for $t > \theta$). At time $t = \theta$, the trap is switched off, so that for $t > \theta$, $k_t = 0$ and $\beta = 0$, and [Equation 15](#) simplifies into:

$$\ddot{x}_m = -a\dot{x}_m \quad \text{Eq. 17}$$

where $a = 1/\tau + 1/T$. Let $v_m = \dot{x}_m$ be the velocity of deflection. [Equation 17](#) yields:

$$v_m(t > \theta) = v_m(\theta)e^{-a(t-\theta)} \quad \text{Eq. 18}$$

where $v_m(\theta) = v_m(t=\theta^+)$ is the initial velocity of relaxation. At the onset of relaxation ($t=\theta^+$), the force balance reads $f(\theta) = -C_\eta v_m(\theta)$. Hence:

$$v_m(t > \theta) = -\frac{f(\theta)}{C_\eta}e^{-a(t-\theta)}. \quad \text{Eq. 19}$$

Integrating [Equation 19](#) yields:

$$x_m(t > \theta) = \frac{f(\theta)}{aC_\eta}e^{-a(t-\theta)} + C. \quad \text{Eq. 20}$$

At the onset of relaxation, $x_m = x_m(\theta)$. Plugging this initial condition in [Equation 20](#) yields:

$$x_m(t > \theta) = x_m(\theta) + \frac{f(\theta)}{aC_\eta}(e^{-a(t-\theta)} - 1). \quad \text{Eq. 21}$$

Let the irreversibility index I be the ratio of irreversible deformation over maximal deformation after a pulling time θ . $I(\theta)$ simply reads:

$$I(\theta) = \frac{x_m(t \rightarrow \infty)}{x_m(\theta)} = \frac{x_m(\theta) - f(\theta)/(aC_\eta)}{x_m(\theta)} = 1 - \frac{\tau}{\tau + T} \frac{f(\theta)}{kx_m(\theta)}. \quad \text{Eq. 22}$$

[Equation 16](#) provides the expression for $x_m(\theta)$. Combining [Equations 13](#) and [16](#) also provides the expression of $f(\theta)$. Plugging the explicit expressions of $x_m(\theta)$ and $f(\theta)$ in [Equation 22](#) leads to the irreversibility index $I(\theta)$:

$$I(\theta) = 1 - \frac{\tau}{\tau + T} \frac{A(T/\tau_A - \beta)e^{-\theta/\tau_A} + B(T/\tau_B - \beta)e^{-\theta/\tau_B}}{1 + Ae^{-\theta/\tau_A} + Be^{-\theta/\tau_B}}. \quad \text{Eq. 23}$$

Since we obtained estimates of β , T , and τ (and therefore A , B , τ_A and τ_B) from individual pulling experiments, this expression provides a prediction with no free parameter for $I(\theta)$ (see [Figure 3H](#)).

QUANTIFICATION AND STATISTICAL ANALYSES

All information concerning the statistical details are provided in the main text and in figure legends. This includes the means and standard errors, the nature of error bars, as well as the number of samples analyzed for each experiment (number of junctions, number of animals). All boxplots use the following standards: center lines of boxes show the medians; boxes limits indicate the 25th and 75th percentiles; whiskers extend 1.5 times the interquartile range from the 25th and 75th percentiles. Boxplots were generated using BoxPlotR, developed by the Tyers and Rappaport labs [50].

DATA AND SOFTWARE AVAILABILITY

Data and software presented in this paper have been deposited at Mendeley Data and are available at <http://dx.doi.org/10.17632/my2dcbrf8g.1>.